

# Effect of Chloride Incorporation on the Intermediate Phase and Film Morphology of Methylammonium Lead Halide Perovskites

Saemi Takahashi, Satoshi Uchida,\* and Hiroshi Segawa

Cite This: *ACS Omega* 2023, 8, 42711–42721

Read Online

ACCESS |



Metrics &amp; More



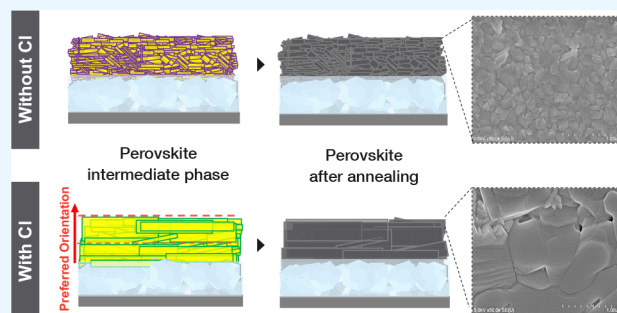
Article Recommendations



Supporting Information

**ABSTRACT:** The influence of chloride integration on perovskite film deposition, encompassing both the structures of intermediate phases and the properties of the final films, was explored. Our methodology involved the fabrication of perovskite intermediate-phase films with varying concentrations of methylammonium chloride (MACl). Subsequently, we conducted an analysis employing X-ray diffraction and Rietveld refinement, incorporating the March-Dollase correction, to gain insights into how chloride-induced intermediate phases impact film morphology. Remarkably, a distinct preferred orientation was observed in the (020) lattice plane perpendicular to the substrate surface, and this orientation was found to be directly correlated to the MACl concentration. This

distinctive arrangement of chloride-induced intermediate-phase complexes facilitated controlled crystallization, leading to highly oriented crystals and an improved film morphology. As a consequence, perovskite solar cell devices incorporating chloride-containing methylammonium lead iodide achieved a power conversion efficiency exceeding 20%. These findings suggest a crucial link between the preferred orientation observed in the final chlorine-derived perovskite films and the intermediate-phase structure formed during the initial stages of perovskite formation. These results suggest a profound impact of intermediate phase compositions and crystal structures on perovskite formation, emphasizing the importance of a comprehensive understanding of these factors to enable precise control over ideal structures and the subsequent transformation into high-quality perovskite films.



## INTRODUCTION

Organic–inorganic halide perovskites, consisting of the structure  $ABX_3$  (where A is a monovalent cation, such as  $CH_3NH_3^+$  (MA),  $CH_2(NH_2)_2^+$  (FA), or  $Cs^+$ ; B stands for Pb (II) or Sn (II); and X stands for iodide, bromide or chloride), have been attracting significant attentions owing to their superior performances in a wide range of optoelectronic applications, along with their cost-effective materials and solution processing.<sup>1–6</sup> Since a perovskite solar cell (PSC) was first reported in 2009 with a power conversion efficiency (PCE) reaching 3.8%,<sup>7</sup> device performance has been improving dramatically in the past decade such that the PCE now exceeds over 25.5%,<sup>8,9</sup> showing great potential for practical applications.

Incorporating chloride species into a perovskite precursor solution is one of the effective strategies to improve perovskite crystal quality and has lately been commanding a great deal of attention again. In fact, most of the recorded efficient PSCs reported in recent years contain excess chloride salts in their precursor solutions.<sup>8,10–12</sup> Although most of the chloride species contained in the precursor solution seem to be dissipated from the final film during a thermal annealing,<sup>13–17</sup> the fabricated perovskite film exhibited an exceedingly improved film coverage with enlarged crystal grains, leading to an improvement of an overall device performance. These

phenomena were confirmed by a number of published papers regardless of the chloride species<sup>1,10,18–20</sup> or deposition methods<sup>21–25</sup> applied in their studies.

While these studies have pointed out the positive effects given by the chloride incorporation, the role of excess chloride species during the perovskite formation process has not been demonstrated enough. The existence of chloride-containing intermediate phases, accompanied by their slow transformation into a perovskite film, has been suggested as a key aspect of chloride-derived perovskites;<sup>15,26–30</sup> however, there are still few studies elucidating the perovskite intermediate phase,<sup>31–35</sup> as well as its transformation process toward final perovskite crystals.<sup>36,37</sup> Besides, those studies currently refer only to the perovskite without chloride inclusion or “ $PbCl_2$  derived perovskite”, which was fabricated from the precursor solution containing  $PbCl_2$  and MAI with a molar ratio of 1:3. As previous studies have shown, the degree of morphological and

Received: July 27, 2023

Revised: October 16, 2023

Accepted: October 18, 2023

Published: November 3, 2023



crystallinity enhancement largely depends on the amount of incorporated chloride materials. Indeed, the most efficient PSCs in the reports were demonstrated with chloride species concentrations much smaller than the perovskite concentration.<sup>12,38,39</sup> As the amount of chloride species in precursor solutions plays a critical role in the eventual film morphology, proposed formation chemistry regarding PbCl<sub>2</sub>-derived MAPbI<sub>3</sub> cannot possibly be applied to the reduced optimal MAcl additives. Hence, a systematic study revealing the correlation between the introduced amount of chloride species and the following structures of intermediate phases, as well as the final perovskite films, need to be further explored.

In this study, the effect of MAcl incorporation in the precursor solution was examined with MAPbI<sub>3</sub> films and PSC devices. First, the spun perovskite film without thermal annealing was fabricated, and its diffraction pattern was analyzed by Rietveld refinement with the March–Dollase function. The perovskite intermediate phase showed a strong preferred orientation depending on the MAcl concentration in the precursor solution. This observation implies that the preferred orientation characteristics mainly observed in chlorine-derived perovskite films are possibly determined at the initial stage of perovskite formation by the geometrical arrangement of the intermediate-phase complex given by the specific interaction of chloride atoms. Then, with an optimized MAcl additive, a MAPbI<sub>3</sub> film was successfully fabricated with an enhance larger grain size, less grain boundaries, and a high degree of crystallinity, which enhanced the optoelectronic properties and resulted in the improvement of device PCE over 20%.

## EXPERIMENTAL METHODS

**Materials.** All of the materials are employed as received without any purification. The chemicals for preparing perovskites were bought MAI from Dyesol, Ltd; PbI<sub>2</sub> was purchased from Kojundo Chemical Laboratory Co., Ltd; MAcl and magnesium(II) bis(trifluoromethanesulfonyl)imide (Mg(TFSI)<sub>2</sub>) were purchased from Tokyo Chemical Industry (TCI); titanium diisopropoxide bis(acetylacetonate) (75 wt % in isopropanol), lithium bis(trifluoromethanesulfonyl)imide (LiTFSI), 4-*tert*-butylpyridine (*t*BP), and chlorobenzene were purchased from Sigma-Aldrich; the 24 nm particle size TiO<sub>2</sub> paste was bought from JGC C&C; and 2,2',7,7'-tetrakis(*N,N*-di-*p*-methoxy-phenylamine)-9,9'-spirobifluorene (Spiro-OMeTAD) was purchased from Merck. Solvents not mentioned above were obtained from Wako Pure Chemical Industries, Ltd.

**Perovskite Thin Film Fabrication.** In this study, we fabricated MAPbI<sub>3</sub> films with different amounts of MAcl additives. For the preparation of the perovskite films, equimolar amounts of PbI<sub>2</sub> and MAI were dissolved in a solvent mix with DMF and DMSO with a ratio of 9:1 as a precursor solution. For the sample with chloride additives, 0.2 and 0.4 mol equiv of MAcl with respect to MAPbI<sub>3</sub> were dissolved together as the additive. Perovskite thin films were deposited based on a fast deposition crystallization method<sup>40</sup> described below. After dropping the precursor solution, a two-step spin coating with a rotation speed of 1000 rpm for 10 s and that of 5000 rpm for 40 s was conducted to disperse the precursor solution. During the spin coating, 0.6 mL of chlorobenzene was dropped quickly 22 s after the beginning of the spin coating program. The as-spun films were annealed at 70 °C for 1 min, followed by further annealing at 100 °C for

45 min to complete the crystallization. However, for the analysis of the perovskite intermediate phase, as-spun wet films were immediately collected and set to the measurement stage without any annealing.

**PSC Device Fabrication.** FTO glass with a sheet resistance of ~10 ohm per square from Nippon Sheet Glass Co. Ltd. was employed as a transparent conductive substrate. The FTO substrates were cleaned by 10 min of ultrasonication with acetone and 2-propanol, followed by a 10 min UV ozone treatment. A compact layer of TiO<sub>2</sub> was then prepared by the spray pyrolysis method at 430 °C. Before spraying, 7.0 mg of LiTFSI and 13.3 mg of Mg(TFSI)<sub>2</sub> were mixed in 0.3 mL of titanium diisopropoxide bis(acetylacetonate) as a precursor solution. A mesoporous TiO<sub>2</sub> layer was then fabricated with a solution that dispersed TiO<sub>2</sub> (PST-24NR) nanoparticles in ethanol. Samples were spin coated with a rotation speed of 6000 rpm for 30 s and then transferred to a hot plate preheated at 550 °C and annealed for 15 min. For the perovskite precursor solutions, equimolar amounts of PbI<sub>2</sub> and MAI were dissolved in 9:1 mixed DMF and DMSO. For MAcl-derived perovskites, 0.2, 0.4, and 1.0 mol equiv of MAcl with respect to MAPbI<sub>3</sub> were further dissolved together. Perovskite absorber layers were deposited based on the antisolvent method described below. After dropping the precursor solution, a two-step spin coating with a rotation speed of 1000 rpm for 10 s and that of 5000 rpm for 40 s was conducted to disperse the droplets. During the spin coating, 0.6 mL of chlorobenzene was quickly dropped 22 s after the beginning of the program. The as-spun films were annealed at 70 °C for 1 min, followed by further annealing at 100 °C for 45 min. A hole transport layer was then spin coated with a rotation speed of 4000 rpm for 30 s using Spiro-OMeTAD solution with a concentration of 72.3 mg in 1 mL of chlorobenzene. LiTFSI (520 mg/mL in acetonitrile, 17.5 μL) and *t*BP (27.8 μL) were added to the solution before the deposition. At last, an Au electrode was deposited by thermal evaporation. The area of the Au contact was more than 0.18 cm<sup>2</sup>. All fabrication processes and *J*–*V* measurements of the devices were performed in a drying room with a dewpoint temperature of –30 °C.

**Analysis Methods.** Out of plane XRD analysis was conducted with a Bruker D8 Discover diffractometer with Cu Kα radiation ( $\lambda = 1.5406 \text{ \AA}$ ) under voltage and current with values of 40 kV and 50 mA, respectively. Bruker Diffraction TOPAS software was used for the XRD data analysis, including Rietveld refinement. Transmittance, reflectance, and absorbance spectra were obtained with a spectrophotometer (UV3600, Shimadzu). For mass spectroscopy analysis of the perovskite films, inductively coupled plasma mass spectrometry (ICP-MS) was performed using an ICPMS-2030 (Shimadzu) instrument. The measurement was conducted using a calibration curve method where calibration samples with known concentrations were prepared. For the samples, perovskite films with and without thermal annealing were fabricated by the process mentioned above. Then, each film was put into a 0.01% ascorbic acid/DMF solution to dissolve the perovskite films, and the measurement was operated by introducing the solutions to a nebulizer. During the measurements, argon gas was used as the carrier gas and plasma gas. A mixture of argon and oxygen gas (Ar/O<sub>2</sub> = 7:3) was used as the auxiliary gas, and helium gas was used as the collision gas. SEM images were obtained with a field emission scanning electron microscope (SU8000, Hitachi). *J*–*V* curves

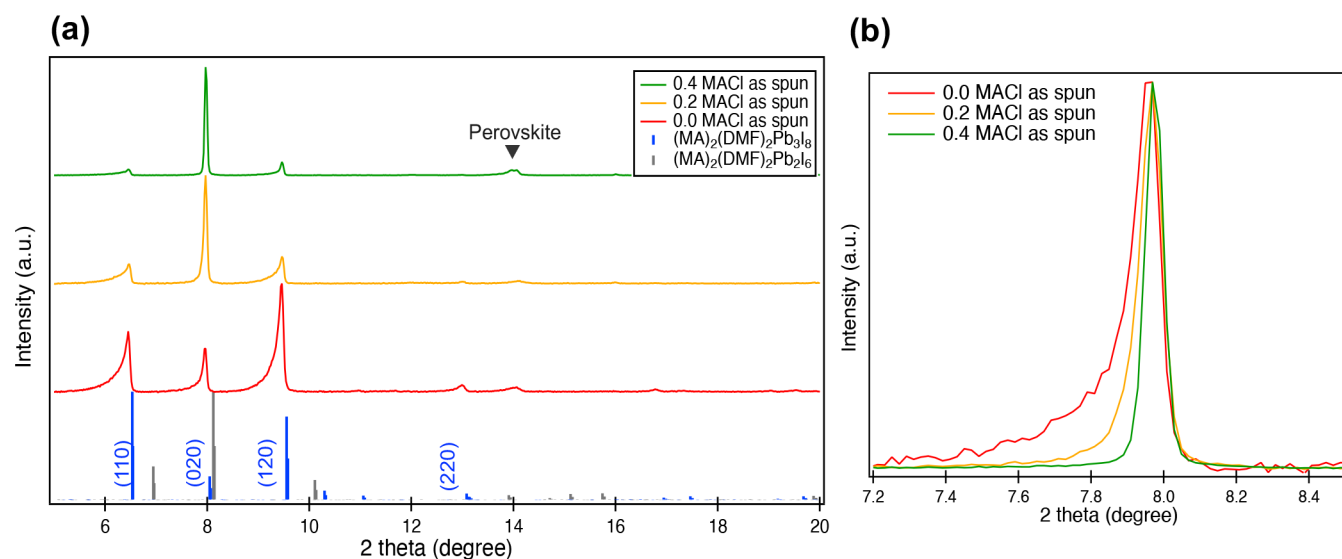


**Figure 1.** (a) XRD patterns of perovskite films without annealing fabricated with each amount of MACl additive and simulated powder diffraction patterns of  $(\text{MA})_2(\text{DMF})_2\text{Pb}_3\text{I}_8$  (blue) and  $(\text{MA})_2(\text{DMF})_2\text{Pb}_2\text{I}_6$  (black). Calculated reflections are summarized in Tables S1 and S2. (b) Enlarged view of the peak around  $8^\circ$ . Intensity is normalized with the peak maximum.

for PSC device evaluation were recorded with a light intensity under AM 1.5 G ( $100 \text{ mW cm}^{-2}$ ) using a 450 W xenon lamp as the light source (YSS-80A; Yamashita Denso Co., Ltd., Japan) and the light intensity was calibrated using a standard Si photodiode of BS-520 (Bunko Keiki Co., Ltd., Japan). Photoluminescence spectrum and photoluminescence quantum yield (PLQY) measurements were performed with the extended absolute photoluminescence quantum yield measurement device (HAMAMATSU C13534, Hamamatsu Photonics). PL lifetimes were measured by a Nanofinder 30 (Tokyo Instruments Inc.) system.

## RESULTS AND DISCUSSION

In order to examine the effect of incorporating different amounts of chloride species in precursor solutions, perovskite films were fabricated and then XRD was immediately measured without thermal annealing. Figure 1(a) shows the XRD patterns of perovskite films fabricated with precursor solutions containing each concentration of MACl. All the spun perovskite films exhibited three conspicuous peaks at the lower degree region. On the other hand, the peak appearing at around  $14^\circ$ , which indicates the (110) face diffraction of tetragonal  $\text{MAPbI}_3$ , showed a significantly low intensity, suggesting that the perovskite crystallized only in trace amounts in all the as-spun films. The structures formed within the perovskite precursor solution are referred to as an intermediate phase, and some solvent-intercalated lead halide structures have been reported for  $\text{MAPbI}_3$  without chloride incorporation using single crystal X-ray diffraction.<sup>31,35,36</sup> Petrov et al.<sup>35</sup> reported three intermediate structures depending on the molar ratio of MAI and  $\text{PbI}_2$ . While our films were primarily fabricated using a precursor solution containing an equimolar proportion of MAI and  $\text{PbI}_2$ , the three dominant peaks detected at angles below  $10^\circ$  in the as-spun films did not align with the peak position of the  $(\text{MA})_2(\text{DMF})_2\text{Pb}_2\text{I}_6$  structure, previously reported as an intermediate phase associated with equimolar MAI and  $\text{PbI}_2$ . Instead, these peaks closely resembled the peak positions observed in  $(\text{MA})_2(\text{DMF})_2\text{Pb}_3\text{I}_8$ , a structure identified in their study as

the intermediate phase structure corresponding to a 1:2 ratio of MAI and  $\text{PbI}_2$ . All of the as-spun perovskite films exhibited nearly identical peak positions. However, Figure 1(b) reveals a slight shift in the peak position with respect to the MACl concentration, suggesting a subtle reduction in lattice size attributable to the incorporation of a small amount of chlorine into the crystal structure.

However, comparing the film diffraction patterns and the calculated powder diffraction pattern of  $(\text{MA})_2(\text{DMF})_2\text{Pb}_3\text{I}_8$ , there is a considerable difference in peak intensity of the capital three peaks, as demonstrated in Figure 1(a). While the calculated powder diffraction pattern has the weakest peak at around  $8^\circ$  that corresponds to the (020) lattice plane, the film without MACl inclusion resulted in the peak corresponding to the (110) lattice plane with the lowest intensity of the three peaks, which is calculated as the strongest intensity in the powder diffraction pattern. Interestingly, by introducing MACl in the precursor solutions, peak intensities of the film diffraction patterns further changed drastically such that the peak corresponding to the (020) lattice plane became much stronger than the other two peaks. Moreover, by increasing the amount of MACl in the precursor solution, the intensity of the (020) peak also increased, indicating that the addition of chloride species has a nontrivial effect on not only the final perovskite film but also the perovskite intermediate phase.

In order to further examine the difference observed in the diffraction patterns of intermediate phase films, Rietveld refinement was performed using the Bruker Diffraction TOPAS software program. The discrepancy in relative peak intensities between the simulated and observed XRD patterns of the  $(\text{MA})_2(\text{DMF})_2\text{Pb}_3\text{I}_8$  intermediate phase suggests the existence of a favored crystal orientation within the as-spun films, likely influenced by the orientation of the intermediate crystallites. Hence, during the Rietveld refinement, we considered and subsequently evaluated the degree of preferred orientation by introducing the March–Dollase method as an intensity correction factor.

The March–Dollase method incorporates an analytical weight function representing the proportion of crystallites

where the reciprocal lattice vectors align with the normal to the surface of the sample:<sup>41,42</sup>

$$P(\alpha) = \frac{1}{N} \sum_{i=1}^N (r^2 \cos^{-1} \alpha + r^2 \sin^{-1} \alpha)^{-3/2} \quad (1)$$

$N$  refers to symmetry equivalent reciprocal lattice points, and  $\alpha$  is the angle between the preferred orientation direction vector and the diffraction plane vector. The preferred orientation parameter  $r$  determines the strength of the preferred orientation, which is defined as the ratio between the correction factors for Bragg peaks perpendicular and parallel to the direction of preferred orientation.<sup>43</sup> Therefore, the March–Dollase function weights different orientations of lattice planes based on the ratio  $r$  and angle  $\alpha$ . When the preferred orientation parameter is 1 ( $r = 1$ ), the weight function is independent of the angle and the material exhibits a random powder orientation, meaning there is no preferred alignment of crystal orientations. On the other hand, when  $r < 1$ , the preferred orientation is exhibited along the direction perpendicular to the surface, while  $r > 1$  indicates a direction parallel to the surface.<sup>41–44</sup>

For the Rietveld refinement,  $(\text{MA})_2(\text{DMF})_2\text{Pb}_3\text{I}_8$ , which corresponded well with the peak position of the perovskite intermediate phase film in Figure 1(a), is used as an initial model structure (Figure 2). The crystal structure parameters

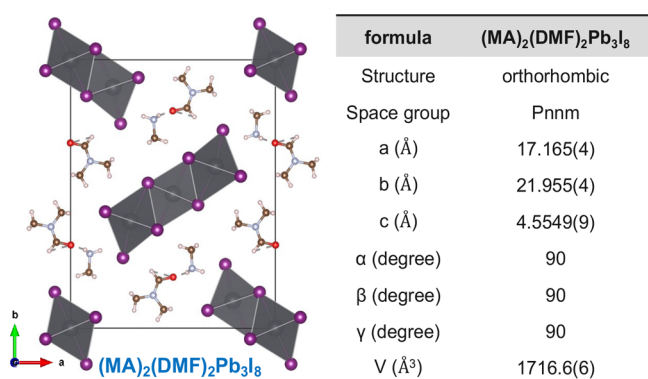


**Figure 2.** Crystal structure of the perovskite intermediate phase used in Rietveld refinement. The unit cell diagram was prepared with a structural model visualization program VESTA<sup>349</sup> based on the crystal structure parameters from the Crystallographic Information File (cif) in ref 35.

were obtained from the Crystallographic Information File (cif) reported in ref 35. Figure 3(a) and (b) show the results of Rietveld refinement for the intermediate phase film fabricated without MACl incorporation with and without considering the effect of the preferred orientation, respectively. Detailed refinement parameters and results for the Rietveld refinement are described in Table S3. As depicted in Figure 3(a) and (b), the measured diffraction pattern, represented by the blue curves, has been fitted to the cumulative calculated curve, indicated by the red curves, which was derived from the identified crystal structure of  $(\text{MA})_2(\text{DMF})_2\text{Pb}_3\text{I}_8$ . Initially, we assigned the  $[2-11]$  direction as the preferred orientation vector, which had been identified in the reference as the preferred orientation direction for the DMSO-containing perovskite intermediate film.<sup>34</sup> In the absence of any preferential orientation correction (Figure 3(a)), both the peak intensity and the ratio of the experimental curve deviated

noticeably from the calculated curve, as previously illustrated in Figure 1(a). However, when considering the preferential orientation through the application of the March–Dollase function, remarkable improvements ensued: the peak intensity ratio approached much closer to the calculated curve, and the residual peak intensities, as depicted below the experimental and calculated curves, significantly diminished (Figure 3(b)). The preferential orientation parameter ( $r$ ) for the  $[2-11]$  direction was calculated as 3.23. It is worth noting that a previously reported paper had documented a value of 5.53 for the DMSO-intercalated intermediate phase.<sup>34</sup> Despite our material being a DMF-induced intermediate phase that differs from the structure employed in the reference, these results suggest that the intermediate phase crystal aligns the  $[2-11]$  face more parallel to the substrate surface, which is in good agreement with their study that the elongated Pb–I network aligns almost parallel to the substrate surface.

However, for the films fabricated with the inclusion of MACl, the preferred orientation toward the  $[2-11]$  direction did not provide a satisfactory fit for both the films with 0.2 and 0.4 mol equiv of MACl. Instead, the intensity of residual peaks corresponding to the (020) lattice plane exhibited a substantial increase with the amount of MACl added, as shown in Figure 4(a). In contrast, the correction of the preferred orientation toward the  $[020]$  direction proved to be considerably more effective for the chloride-induced intermediate phases. As demonstrated in Figure 4(b), the calculated curves fitted well with the experimental curves for both the films with 0.2 and 0.4 mol equiv of MACl, and the peak intensities of the residual curves decreased considerably. The preferred orientation parameter ( $r$ ) was calculated as 0.44 for the film with 0.2 mol equiv of MACl and 0.33 for the film with 0.4 mol equiv of MACl. Detailed parameters and results are summarized in Tables S4 and S5, respectively. Notably, all films exhibited preferred orientation values smaller than 1, indicating a strong characteristic of the (020) faces aligning perpendicular to the sample surface. Furthermore, the degree of preferred orientation toward the  $[020]$  direction increased with the addition of more MACl to the precursor solutions. These results suggest that the addition of chloride species to the precursor solution promotes growth of the (020) lattice plane in a direction more perpendicular to the substrate surface.

This observation strongly aligns with our previous report, where we noted that the (020) lattice plane, containing chlorine atom replacements, exhibits slower growth and has more morphological importance.<sup>45</sup> Assuming that chlorine atoms are substituted with terminal iodine atoms within the lead halide octahedra, in accordance with the reference's structure, these chlorine atoms would also align themselves along the  $b$ -axis direction, which is perpendicular to the substrate surface. As depicted in Figure 5, retarding crystal growth along the  $b$ -axis direction encourages the crystal to expand more toward the  $a$ - and  $c$ -axes. Consequently, this leads to the enlargement of the (020) faces in the final film. While the previous report primarily focused on calculations with and without chloride inclusion, the experimental film diffraction patterns, coupled with the variations in the degree of preferred orientation in response to the MACl concentration, provide empirical support for the emergence of chlorine-induced lattice planes and their heightened morphological significance.

The emergence of highly oriented perovskite intermediate phases can be correlated to the enhanced crystallinity of the final perovskite films. As depicted in Figure 6(a), the XRD

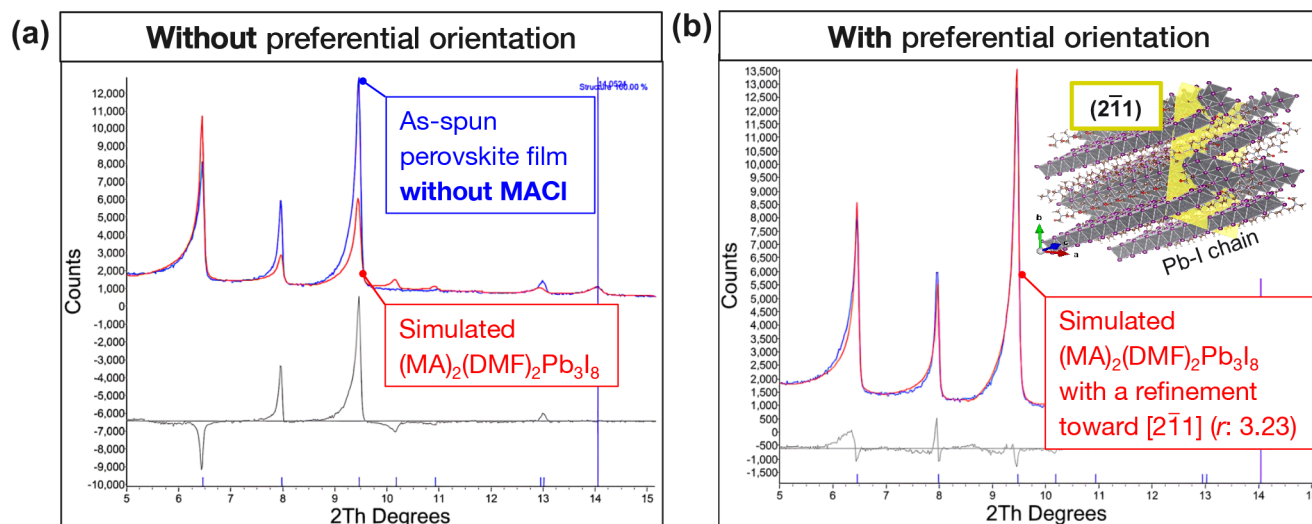


**Figure 3.** Diffraction patterns of intermediate phase without MACl inclusion after Rietveld refinement (a) without a preferential orientation and (b) with a preferred orientation. The inset crystal structure diagram shows the  $(2-11)$  face of  $(\text{MA})_2(\text{DMF})_2\text{Pb}_3\text{I}_8$ .

diffraction patterns of the final perovskite films, which were prepared from precursor solutions containing varying amounts of MACl, consistently exhibited diffraction patterns closely matching the tetragonal  $\text{MAPbI}_3$  structure.<sup>46</sup> Notably, apart from the three peaks attributed to the FTO substrates, no peaks associated with intermediate phases or precursor materials, such as MAI,  $\text{PbI}_2$ , MACl, or  $\text{PbCl}_2$ , were observed. Evidently, the majority of chloride species present in the precursor solutions or within the as-spun films were effectively eliminated during the thermal annealing process. Consequently, all films underwent a successful transformation into perovskites with no observable shift in peak positions, as illustrated in Figure 6(b). This phenomenon is further supported by optical absorption spectroscopy (Figure S1), where all perovskite films exhibited nearly identical absorption edges at approximately 800 nm, as also confirmed by the Tauc plot in Figure 6(c). The band gap energies of perovskite films prepared with 0.0, 0.2, and 0.4 mol equiv of MACl were estimated to be 1.600, 1.601, and 1.604 eV, respectively. These values indicate minimal variation in band gaps, although a slight blue shift was observed in the MACl-induced films, possibly attributable to trace amounts of the remaining chlorine atoms within the perovskite lattice.

Furthermore, an analysis using inductively coupled plasma mass spectrometry (ICP-MS), summarized in Figure 6(d) and Table S6, verified the presence of chlorine atoms in the as-spun perovskite films, initially at concentrations comparable to those in the precursor solutions. However, after the thermal annealing process, there was a substantial reduction in the quantity of chlorine atoms, while the iodine atom content exhibited a minimal change. Simultaneously, there was a slight increase in the amount of chlorine atoms in the final perovskite films induced by MACl, which can account for the observed slight blue shift in the band gap energy in the Tauc plot in Figure 6(c). This suggests that a very small quantity of chlorine atoms may remain within the perovskite lattice in these films, and this quantity may increase with higher MACl concentrations in the precursor solution.<sup>13,17</sup> Since the perovskite films were annealed under the same conditions as those without chlorine incorporation, this issue may be addressed by optimizing the annealing conditions for chlorine-induced

perovskite films, such as increasing the annealing temperature or duration. Nonetheless, these observations unequivocally demonstrate the formation of chlorine-containing intermediate phases during the initial stages of perovskite fabrication, followed by a transformation into perovskite with the removal of chlorine species during the annealing process.<sup>16,37</sup>

Despite the negligible differences in the perovskite compositions, MACl-induced perovskite films exhibited a pronounced preferred orientation. In contrast, the perovskite film without MACl inclusion displayed a diffraction pattern that corresponded well to randomly oriented tetragonal  $\text{MAPbI}_3$ , owing to the rapid crystallization characteristic induced by the antisolvent deposition technique. Conversely, with the introduction of an excess of MACl into the precursor solutions, two reflection peaks at approximately  $14^\circ$  and  $28^\circ$ , corresponding to the (110) and (220) lattice planes of tetragonal  $\text{MAPbI}_3$ ,<sup>46</sup> became more prominent than other reflection peaks. This distinctive feature intensified with increasing amounts of MACl, as depicted in Figure S2. This strong preferred orientation characteristic observed in MACl-incorporated perovskite films aligns with the increasing degree of preferred orientation observed in intermediate films, as demonstrated in Figures 1(a). The substantial preferred orientation of [020] planes within the perovskite intermediate phase oriented perpendicular to the substrate, likely due to the replacement of chlorine atoms with terminal iodine atoms within the lead halide octahedra along the *b*-axis,<sup>45</sup> undergoes transformation into  $\text{MAPbI}_3$  during thermal annealing. Consequently, this may result in a pronounced preferred orientation of the (010) lattice plane in cubic  $\text{MAPbI}_3$  and subsequently of the (110) lattice plane in tetragonal  $\text{MAPbI}_3$  after the thermal annealing process.

The formation of highly crystalline perovskite films, derived from a precursor solution incorporating MACl, is further confirmed through a comparison of the surface morphology in each perovskite film. Figure 7(a) presents top-view surface SEM images of perovskite films prepared with precursor solutions containing 0, 0.2, and 0.4 mol equiv of MACl relative to  $\text{MAPbI}_3$ . The grain size distributions of the perovskite films exhibit significant enhancement as the quantity of incorporated MACl increases, aligning with prior research on chloride

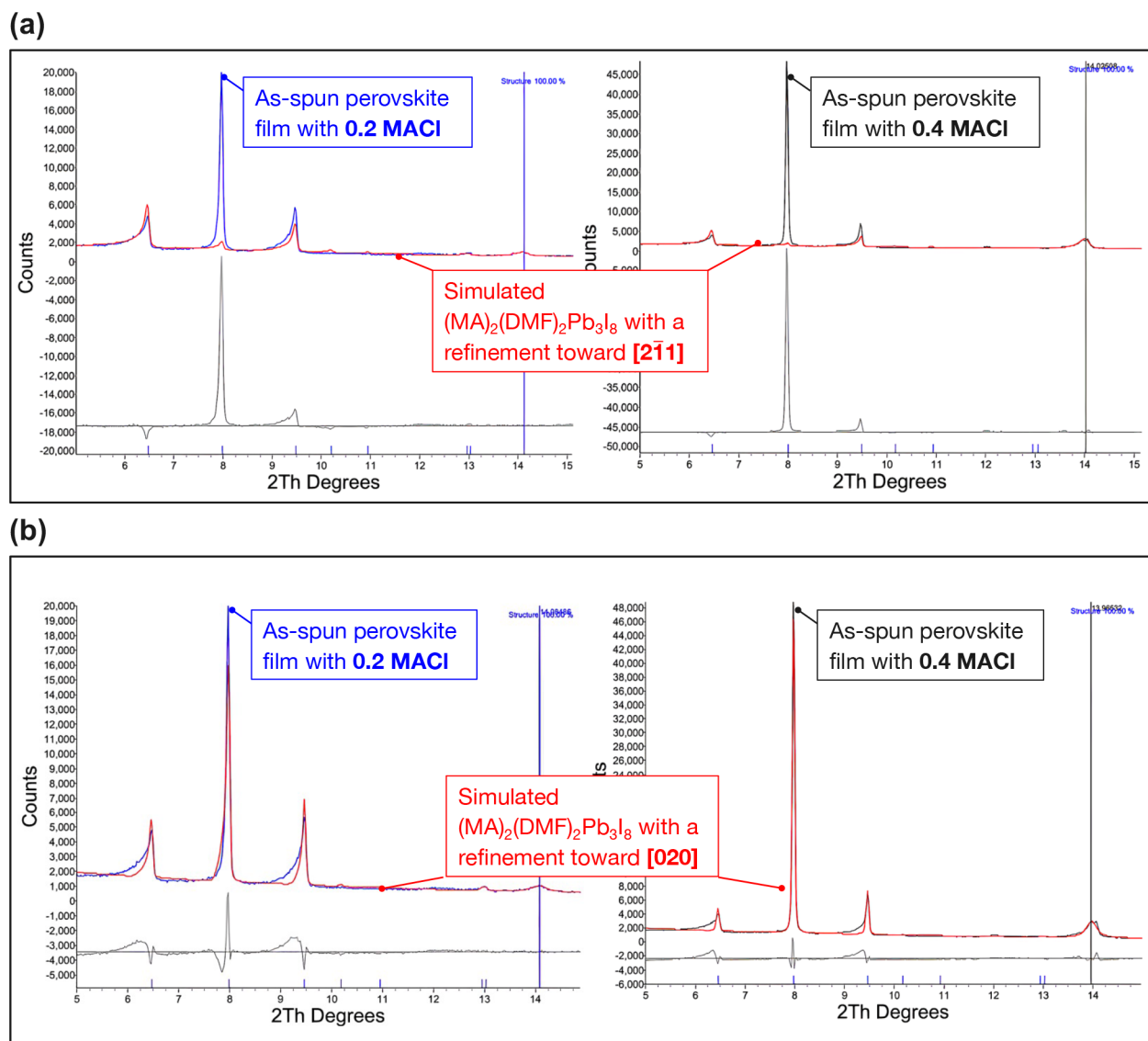


**Figure 4.** Rietveld refinement of the diffraction patterns of the perovskite intermediate phase with 0.2 and 0.4 MACI. (a) Refinement with a preferential orientation toward the  $[2-11]$  direction and the preferred orientation parameter  $r = 3.23$ . (b) Rietveld refinement with a preferential orientation toward the  $[020]$  direction. The preferred orientation parameter  $r$  was calculated as 0.44 for 0.2 MACI (left) and 0.33 for 0.4 MACI (right).

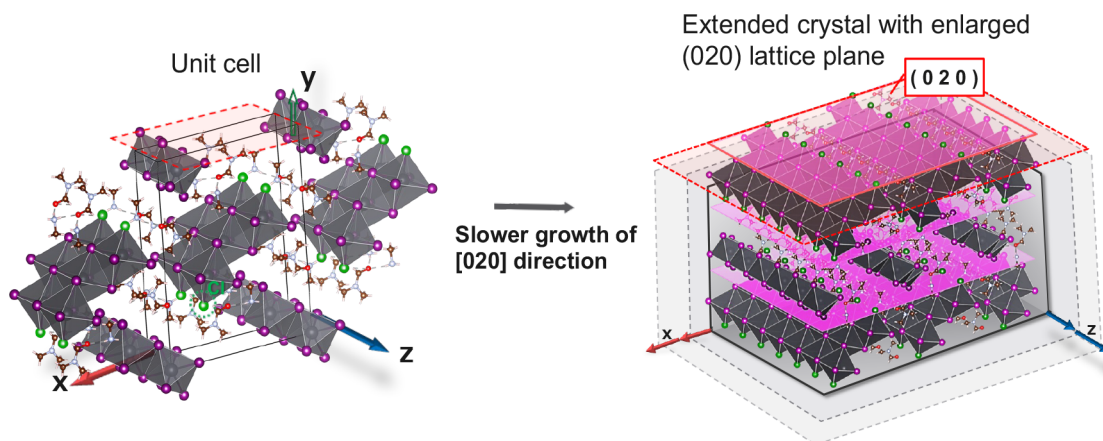


**Figure 5.** Schematic illustration of the growth of the specific lattice plane in a chloride-induced perovskite intermediate phase crystal. Hydrogen atoms are omitted for clarity. Chloride atoms (green) are aligned toward the  $b$ -axis, which was calculated as the most feasible growth plane in the reference.

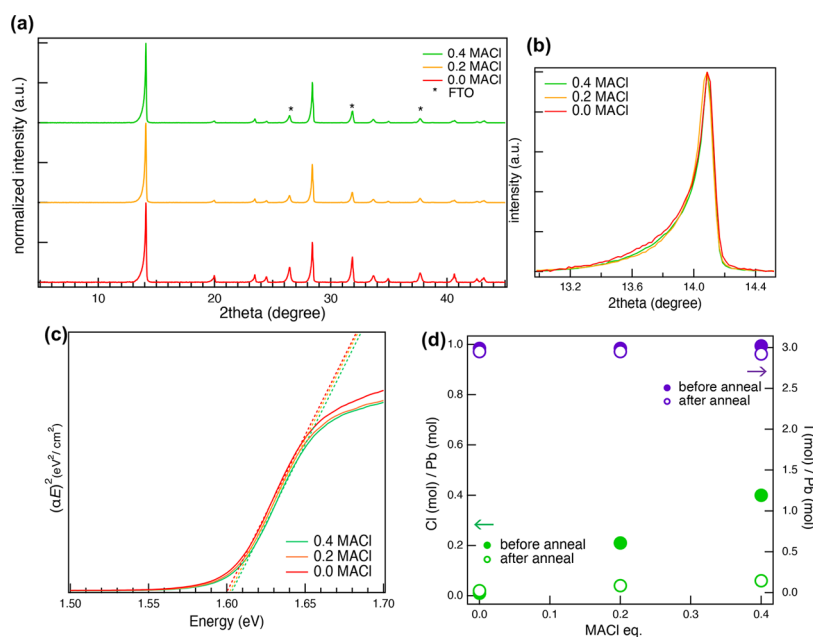


**Figure 6.** (a) XRD patterns, (b) enlarged view of the XRD peaks corresponding to the (110) lattice plane, (c) Tauc plot, and (d) molar ratio of iodine and chlorine atoms to lead atoms concerning thermal annealing for perovskite films prepared with 0.0, 0.2, and 0.4 mol equiv of MACl.

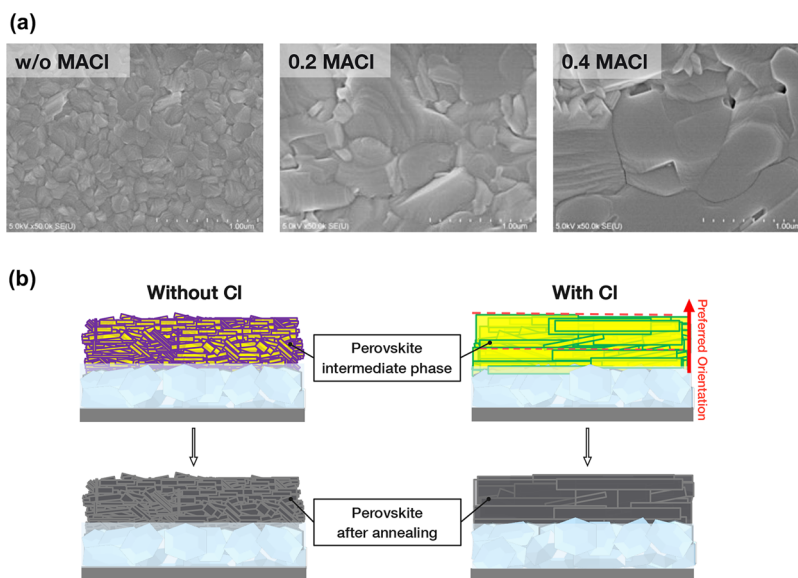


**Figure 7.** (a) Top-view SEM images of perovskite films fabricated with 0.0, 0.2, and 0.4 mol equiv of MACl. (b) Schematic illustration of the transformation of the perovskite intermediate phase into the perovskite with and without chloride inclusion.

incorporation in perovskite formation.<sup>16,29,38</sup> While the film without MACl displayed an average grain size of approximately 300 nm, the film prepared with 0.2 mol equiv of MACl exhibited an enlarged grain size exceeding 500 nm. In the case of the film with 0.4 mol equiv of MACl, the grain sizes exceeded 1.00  $\mu\text{m}$ . This observation corroborates the earlier XRD results in Figure 6(a), indicating that perovskite films with a higher degree of crystallinity are obtained due to the inclusion of MACl in precursor solutions.

The enhanced crystallinity achieved through chloride-induced perovskite films originating from highly oriented intermediate phases implies that controlling the growth direction of an intermediate phase plays a pivotal role in influencing the perovskite morphology. As mentioned previously, the horizontal orientation of Pb–I chains in

perovskite intermediate phase crystals emerges as a crucial factor for fabricating perovskite films with superior morphology.<sup>34</sup> As schematically illustrated in Figure 7(b), in contrast to perovskite films without chloride inclusion that crystallize with smaller crystallites, the aligned chlorine atoms further promote the growth of the intermediate phase well oriented perpendicular to the substrate surface. Then transformation of perovskite intermediate phase to perovskite film will occur by gradually substituting iodine atoms during thermal annealing, and this transformation will ultimately lead to the formation of highly crystallized perovskite films.

Finally, to examine the influence of the chloride incorporations on device performances, PSC devices in the architecture of fluorine-doped tin oxide (FTO)/compact  $\text{TiO}_2$ /mesoporous  $\text{TiO}_2$ /perovskite/Spiro-MeOTAD/Au

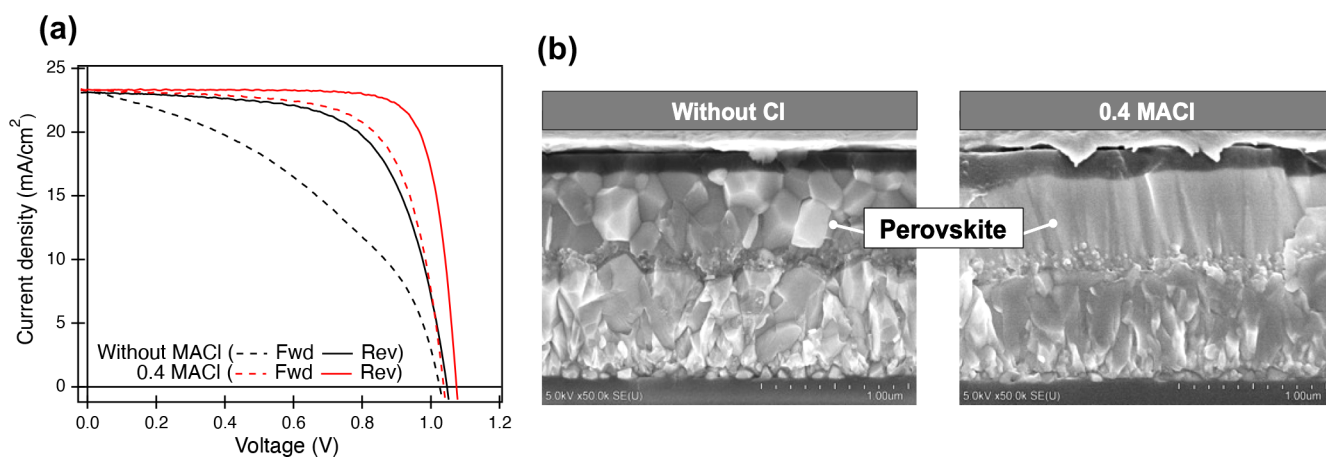


**Figure 8.** (a)  $I$ – $V$  curves of the PSC devices fabricated with the perovskite film with and without MACI. (b) Cross-sectional SEM images of PSC devices fabricated without MACI and with 0.4 mol equiv of MACI.

were fabricated and characterized. Perovskite layers were prepared with the process as the films demonstrated in previously noted measurements.

Figure 8(a) shows the  $I$ – $V$  characteristics of the best PSC devices prepared with perovskite films with and without MACI. Corresponding photovoltaic parameters of each device are summarized in Table 1. The device prepared without MACI

**Table 1. Photovoltaic Parameters of the Best-Performing PSCs Prepared with and without MACI**

sample	scan	$J_{sc}$ (mA cm <sup>-2</sup> )	$V_{oc}$ (V)	FF (–)	PCE (%)
without MACI	fwd	23.2	1.03	0.42	10.0
	rev	23.1	1.05	0.65	15.8
with 0.4 mol equiv of MACI	fwd	23.3	1.04	0.69	16.7
	rev	23.3	1.07	0.80	20.0

incorporation showed a power conversion efficiency (PCE) of 15.8% with hysteresis. An addition excess MACI in the perovskite precursor solution resulted in improved device performance and achieved a maximum PCE over 20% with the device with 0.4 mol equiv MACI. Detailed distributions of each photovoltaic parameters of the PSC devices for several batches with the corresponding MACI ratio are also shown in Figure S3. Distributions of short circuit current density ( $J_{sc}$ ) values did not show an evident difference between the amount of MACI included in the perovskite deposition, which was also confirmed by the EQE measurement shown in Figure S4. It is rather consistent with the trends observed in the above-mentioned UV–vis absorption and XRD results, where almost no notable shift was observed in either the absorption edge or lattice constant between the perovskite films, indicating that all films were most likely to be transformed into MAPbI<sub>3</sub>. Distribution of open circuit voltage ( $V_{oc}$ ) values showed similar trends between the devices prepared with 0.0, 0.2, and 0.4 mol equiv of MACI, although the device prepared with 1.0 mol equiv of MACI had comparatively poorer  $V_{oc}$  values. Meanwhile, however, distributions of fill factor (FF) values showed a trend that is close to that of PCE distributions. An outstanding improvement of FF values from 0.65 to 0.80 appeared with the incorporation of 0.4 mol equiv of MACI compared to that of the device without MACI included. However, further addition of MACI resulted in a decrease in

FF value with the device with 1.0 MACI, which is in good agreement with the drop that appeared at PCE values. These results suggest that MACI incorporation in the perovskite precursor solution significantly affected the device performance, and an enhancement of the device performance is most likely to be attributed to the improvement of FF values.

Figure 8(b) shows cross-sectional SEM images of the PSC devices fabricated with perovskite films with and without MACI. Additional SEM images for other compositions are summarized in Figure S5. In all devices, the thickness of each perovskite film remained nearly constant, typically around 500 to 550 nm. However, as the amount of MACI increased, the surface of the perovskite film exhibited reduced uniformity. Particularly in the case of the device with 1.0 mol equiv of MACI, the subsequent Spiro-OMeTAD layer displayed variations in thickness, which account for the earlier-mentioned decline in device performance. This could be attributed to the slower crystal growth resulting from a higher level of MACI incorporation, preventing the rapid crystallization typically induced by the antisolvent deposition and thereby hindering uniform crystallization. However, at the same time, distinct differences emerged in the perovskite microstructure. The device fabricated with the perovskite film without MACI incorporation exhibited small grains and noticeable grain boundaries in various directions. Conversely, in the device with MACI incorporation, grain boundaries primarily oriented vertically were reduced and were nearly negligible. The reduction in grain boundaries observed in the devices with MACI-induced perovskite films appears to be closely linked with the enlargement of perovskite grains, consistent with the results observed in top-view SEM images in Figure 7(a). It is well-established that the grain boundaries can serve as trap centers, leading to unfavorable charge recombination; thus, they have a significant influence on device performance.<sup>47,48</sup> Therefore, the device fabricated with the perovskite film containing fewer grain boundaries is anticipated to exhibit superior carrier transport, leading to better device performance.

Additionally, we performed an analysis of the photoluminescence (PL) spectra and corresponding decay curves for the perovskite films prepared with varying amounts of MACI. To eliminate any potential influence from electron injection into TiO<sub>2</sub>, we deposited perovskite films onto quartz substrates. As demonstrated in Figure S6(a), the PL peaks

exhibited a slight shift toward shorter wavelengths with the inclusion of MAI. This aligns with the results observed in the absorption spectra and is likely due to the presence of residual small amounts of chlorine atoms.

Moreover, the perovskite film without MAI incorporation exhibited a broader PL spectrum in comparison to that of the film with MAI, indicating a higher possibility of nonradiative recombination. This observation is further substantiated by the overall PL quantum yield (PLQY), where the perovskite film with MAI exhibits a significantly higher PLQY value. This suggests a more efficient radiative recombination process with fewer traps or defects in the perovskite films. The corresponding decay curves, detailed in Table S6(b), also illustrate that MAI incorporation during perovskite deposition enhances the carrier lifetime, which effectively accounts for the substantial enhancement in the device performance observed in devices fabricated with and without MAI incorporation. It has been proposed that high-quality films are associated with extended PL lifetimes, while grain boundaries tend to exhibit lower PL intensity and faster nonradiative decay rates.<sup>48</sup> The fabrication of highly crystalline perovskite films with fewer grain boundaries appears to have reduced these nonradiative pathways, underscoring the benefits of chloride incorporation in perovskite fabrication.

## CONCLUSION

In summary, this study explored the consequences of incorporating chloride additives during perovskite deposition, examining both the intermediate phase structures and the properties of the final perovskite films. Perovskite intermediate-phase films were created by varying the concentration of MAI, then characterized through XRD measurements and Rietveld refinement by employing the March–Dollase correction. The chloride-induced intermediate phase displayed a distinct preferred orientation, namely, the (020) face, oriented perpendicular to the substrate surface, with a correlation observed with the MAI concentration. This unique configuration of the chloride-induced intermediate phase appears to exert a significant influence on controlled crystallization, resulting in highly oriented crystals and enhanced film morphology. These improvements ultimately led to power conversion efficiencies exceeding 20% in perovskite solar cell devices. This observation suggests a connection between the preferred orientation characteristics observed in the final chlorine-derived perovskite films and the intermediate phase structure formed during the initial stages of perovskite formation. Our findings underscore the substantial impact of intermediate-phase compositions and crystal structures on perovskite formation, which in turn dictate the quality of the resulting perovskite films. Consequently, a deeper understanding of these factors is pivotal for achieving precise control over ideal crystal structures and facilitating their transformation into high-quality perovskite films.

## ASSOCIATED CONTENT

### Supporting Information

The Supporting Information is available free of charge at <https://pubs.acs.org/doi/10.1021/acsomega.3c05463>.

Additional experimental details and methods (PDF)

## AUTHOR INFORMATION

### Corresponding Author

Satoshi Uchida – Research Center for Advanced Science and Technology, The University of Tokyo, Meguro-ku, Tokyo 153-8904, Japan; [orcid.org/0000-0002-4971-574X](https://orcid.org/0000-0002-4971-574X); Phone: +81- 3-5452-5298; Email: [uchida@rcast.u-tokyo.ac.jp](mailto:uchida@rcast.u-tokyo.ac.jp)

### Authors

Saemi Takahashi – Research Association for Technology Innovation of Organic Photovoltaics (RATO), Meguro-ku, Tokyo 153-8904, Japan; Department of General Systems Studies, Graduate School of Arts and Sciences, The University of Tokyo, Meguro-ku, Tokyo 153-8902, Japan; [orcid.org/0000-0002-2606-3822](https://orcid.org/0000-0002-2606-3822)

Hiroshi Segawa – Research Association for Technology Innovation of Organic Photovoltaics (RATO), Meguro-ku, Tokyo 153-8904, Japan; Research Center for Advanced Science and Technology, The University of Tokyo, Meguro-ku, Tokyo 153-8904, Japan; Department of General Systems Studies, Graduate School of Arts and Sciences, The University of Tokyo, Meguro-ku, Tokyo 153-8902, Japan; [orcid.org/0000-0001-8076-9722](https://orcid.org/0000-0001-8076-9722)

Complete contact information is available at:

<https://pubs.acs.org/10.1021/acsomega.3c05463>

### Notes

The authors declare no competing financial interest.

## ACKNOWLEDGMENTS

This paper is based on results obtained from a project, JPNP21016, commissioned by the New Energy and Industrial Technology Development Organization (NEDO). Additionally, this work was supported by JST SPRING, Grant JPMJSP2108.

## REFERENCES

- (1) Lee, M. M.; Teuscher, J.; Miyasaka, T.; Murakami, T. N.; Snaith, H. J. Efficient Hybrid Solar Cells Based on Meso-Superstructured Organometal Halide Perovskites. *Science* **2012**, *338* (6107), 643–647.
- (2) Kim, H. S.; Lee, C. R.; Im, J. H.; Lee, K. B.; Moehl, T.; Marchioro, A.; Moon, S. J.; Humphry-Baker, R.; Yum, J. H.; Moser, J. E.; Grätzel, M.; Park, N. G. Lead Iodide Perovskite Sensitized All-Solid-State Submicron Thin Film Mesoscopic Solar Cell with Efficiency Exceeding 9%. *Sci. Rep.* **2012**, *2*, 591.
- (3) Saidaminov, M. I.; Adinolfi, V.; Comin, R.; Abdelhady, A. L.; Peng, W.; Dursun, I.; Yuan, M.; Hoogland, S.; Sargent, E. H.; Bakr, O. M. Planar-Integrated Single-Crystalline Perovskite Photodetectors. *Nat. Commun.* **2015**, *6*, 8724.
- (4) Gong, X.; Yang, Z.; Walters, G.; Comin, R.; Ning, Z.; Beauregard, E.; Adinolfi, V.; Voznyy, O.; Sargent, E. H. Highly Efficient Quantum Dot Near-Infrared Light-Emitting Diodes. *Nat. Photonics* **2016**, *10* (4), 253–257.
- (5) Cho, H.; Jeong, S. H.; Park, M. H.; Kim, Y. H.; Wolf, C.; Lee, C. L.; Heo, J. H.; Sadhanala, A.; Myoung, N. S.; Yoo, S.; Im, S. H.; Friend, R. H.; Lee, T. W. Overcoming the Electroluminescence Efficiency Limitations of Perovskite Light-Emitting Diodes. *Science* **2015**, *350* (6265), 1222–1225.
- (6) Saliba, M.; Wood, S. M.; Patel, J. B.; Nayak, P. K.; Huang, J.; Alexander-Webber, J. A.; Wenger, B.; Stranks, S. D.; Hörlantner, M. T.; Wang, J. T. W.; Nicholas, R. J.; Herz, L. M.; Johnston, M. B.; Morris, S. M.; Snaith, H. J.; Riede, M. K. Structured Organic-Inorganic Perovskite toward a Distributed Feedback Laser. *Adv. Mater.* **2016**, *28* (5), 923–929.

- (7) Kojima, A.; Teshima, K.; Shirai, Y.; Miyasaka, T. Organometal Halide Perovskites as Visible-Light Sensitizers for Photovoltaic Cells. *J. Am. Chem. Soc.* **2009**, *131* (17), 6050–6051.
- (8) Kim, G.; Min, H.; Lee, K. S.; Lee, D. Y.; Yoon, S. M.; Seok, S. I. Impact of Strain Relaxation on Performance of A-Formamidinium Lead Iodide Perovskite Solar Cells. *Science* **2020**, *370* (6512), 108–112.
- (9) Yoo, J. J.; Seo, G.; Chua, M. R.; Park, T. G.; Lu, Y.; Rotermund, F.; Kim, Y.; Moon, C. S.; Jeon, N. J.; Correa-Baena, J.-P.; Bulović, V.; Shin, S. S.; Bawendi, M. G.; Seo, J. Efficient Perovskite Solar Cells via Improved Carrier Management. *Nature* **2021**, *590* (7847), 587–593.
- (10) Min, H.; Kim, M.; Lee, S. U.; Kim, H.; Kim, G.; Choi, K.; Lee, J. H.; Seok, S. I. Efficient, Stable Solar Cells by Using Inherent Bandgap of a-Phase Formamidinium Lead Iodide. *Science* **2019**, *366* (6466), 749–753.
- (11) Jung, E. H.; Jeon, N. J.; Park, E. Y.; Moon, C. S.; Shin, T. J.; Yang, T.-Y.; Noh, J. H.; Seo, J. Efficient, Stable and Scalable Perovskite Solar Cells Using Poly (3-Hexylthiophene). *Nature* **2019**, *567* (7749), 511–515.
- (12) Kim, M.; Kim, G.-H.; Lee, T. K.; Choi, I. W.; Choi, H. W.; Jo, Y.; Yoon, Y. J.; Kim, J. W.; Lee, J.; Huh, D.; Lee, H.; Kwak, S. K.; Kim, J. Y.; Kim, D. S. Methylammonium Chloride Induces Intermediate Phase Stabilization for Efficient Perovskite Solar Cells. *Joule* **2019**, *3* (9), 2179–2192.
- (13) Cojocaru, L.; Uchida, S.; Jena, A. K.; Miyasaka, T.; Nakazaki, J.; Kubo, T.; Segawa, H. Determination of Chloride Content in Planar  $\text{CH}_3\text{NH}_3\text{PbI}_{3-x}\text{Cl}_x$  Solar Cells by Chemical Analysis. *Chem. Lett.* **2015**, *44* (8), 1089–1091.
- (14) Colella, S.; Mosconi, E.; Pellegrino, G.; Alberti, A.; Guerra, V. L. P.; Masi, S.; Listorti, A.; Rizzo, A.; Condorelli, G. G.; de Angelis, F.; Gigli, G. Elusive Presence of Chloride in Mixed Halide Perovskite Solar Cells. *J. Phys. Chem. Lett.* **2014**, *5* (20), 3532–3538.
- (15) Unger, E. L.; Bowring, A. R.; Tassone, C. J.; Pool, V. L.; Gold-Parker, A.; Checharoen, R.; Stone, K. H.; Hoke, E. T.; Toney, M. F.; McGehee, M. D. Chloride in Lead Chloride-Derived Organo-Metal Halides for Perovskite-Absorber Solar Cells. *Chem. Mater.* **2014**, *26* (24), 7158–7165.
- (16) Williams, S. T.; Zuo, F.; Chueh, C. C.; Liao, C. Y.; Liang, P. W.; Jen, A. K. Y. Role of Chloride in the Morphological Evolution of Organo-Lead Halide Perovskite Thin Films. *ACS Nano* **2014**, *8* (10), 10640–10654.
- (17) Cojocaru, L.; Uchida, S.; Matsubara, D.; Matsumoto, H.; Ito, K.; Otsu, Y.; Chapon, P.; Nakazaki, J.; Kubo, T.; Segawa, H. Direct Confirmation of Distribution for  $\text{Cl}^-$  in  $\text{CH}_3\text{NH}_3\text{PbI}_{3-x}\text{Cl}_x$  Layer of Perovskite Solar Cells. *Chem. Lett.* **2016**, *45* (8), 884–886.
- (18) Tavakoli, M. M.; Yadav, P.; Prochowicz, D.; Sponseller, M.; Osherov, A.; Bulović, V.; Kong, J. Controllable Perovskite Crystallization via Antisolvent Technique Using Chloride Additives for Highly Efficient Planar Perovskite Solar Cells. *Adv. Energy Mater.* **2019**, *9* (17), 1803587.
- (19) Li, Q.; Zhao, Y.; Fu, R.; Zhou, W.; Zhao, Y.; Liu, X.; Yu, D.; Zhao, Q. Efficient Perovskite Solar Cells Fabricated Through CsCl-Enhanced  $\text{PbI}_2$  Precursor via Sequential Deposition. *Adv. Mater.* **2018**, *30* (40), 1803095.
- (20) Murugan, V.; Ogomi, Y.; Pandey, S. S.; Toyoda, T.; Shen, Q.; Hayase, S. Effects of Different Chloride Precursors on Crystal Growth of Lead Halide Perovskites. *Appl. Phys. Express* **2015**, *8* (12), 125501.
- (21) Nie, W.; Tsai, H.; Asadpour, R.; Blancon, J.-C.; Neukirch, A. J.; Gupta, G.; Crochet, J. J.; Chhowalla, M.; Tretiak, S.; Alam, M. A.; Wang, H.-L.; Mohite, A. D. High-Efficiency Solution-Processed Perovskite Solar Cells with Millimeter-Scale Grains. *Science* **2015**, *347* (6221), 522–526.
- (22) Zhao, Y.; Zhu, K.  $\text{CH}_3\text{NH}_3\text{Cl}$ -Assisted One-Step Solution Growth of  $\text{CH}_3\text{NH}_3\text{PbI}_3$ : Structure, Charge-Carrier Dynamics, and Photovoltaic Properties of Perovskite Solar Cells. *J. Phys. Chem. C* **2014**, *118* (18), 9412–9418.
- (23) Liu, M.; Johnston, M. B.; Snaith, H. J. Efficient Planar Heterojunction Perovskite Solar Cells by Vapour Deposition. *Nature* **2013**, *501* (7467), 395–398.
- (24) Chen, Q.; Zhou, H.; Fang, Y.; Stieg, A. Z.; Song, T.-B.; Wang, H. H.; Xu, X.; Liu, Y.; Lu, S.; You, J.; Sun, P.; McKay, J.; Goorsky, M. S.; Yang, Y. The Optoelectronic Role of Chlorine in  $\text{CH}_3\text{NH}_3\text{PbI}_3$  (Cl)-Based Perovskite Solar Cells. *Nat. Commun.* **2015**, *6*, 7269.
- (25) Docampo, P.; Hanusch, F. C.; Stranks, S. D.; Döblinger, M.; Feckl, J. M.; Ehrensperger, M.; Minar, N. K.; Johnston, M. B.; Snaith, H. J.; Bein, T. Solution Deposition-Conversion for Planar Heterojunction Mixed Halide Perovskite Solar Cells. *Adv. Energy Mater.* **2014**, *4* (14), 1400355.
- (26) Yu, H.; Wang, F.; Xie, F.; Li, W.; Chen, J.; Zhao, N. The Role of Chlorine in the Formation Process of “ $\text{CH}_3\text{NH}_3\text{PbI}_{3-x}\text{Cl}_x$ ” Perovskite. *Adv. Funct. Mater.* **2014**, *24* (45), 7102–7108.
- (27) Nenon, D. P.; Christians, J. A.; Wheeler, L. M.; Blackburn, J. L.; Sanehira, E. M.; Dou, B.; Olsen, M. L.; Zhu, K.; Berry, J. J.; Luther, J. M. Structural and Chemical Evolution of Methylammonium Lead Halide Perovskites during Thermal Processing from Solution. *Energy Environ. Sci.* **2016**, *9* (6), 2072–2082.
- (28) Yantara, N.; Yanan, F.; Shi, C.; Dewi, H. A.; Boix, P. P.; Mhaisalkar, S. G.; Mathews, N. Unravelling the Effects of Cl Addition in Single Step  $\text{CH}_3\text{NH}_3\text{PbI}_3$  Perovskite Solar Cells. *Chem. Mater.* **2015**, *27* (7), 2309–2314.
- (29) Fan, L.; Ding, Y.; Luo, J.; Shi, B.; Yao, X.; Wei, C.; Zhang, D.; Wang, G.; Sheng, Y.; Chen, Y.; Hagfeldt, A.; Zhao, Y.; Zhang, X. Elucidating the Role of Chlorine in Perovskite Solar Cells. *J. Mater. Chem. A* **2017**, *5* (16), 7423–7432.
- (30) Moore, D. T.; Sai, H.; Tan, K. W.; Smilgies, D. M.; Zhang, W.; Snaith, H. J.; Wiesner, U.; Estroff, L. A. Crystallization Kinetics of Organic-Inorganic Trihalide Perovskites and the Role of the Lead Anion in Crystal Growth. *J. Am. Chem. Soc.* **2015**, *137* (6), 2350–2358.
- (31) Wakamiya, A.; Endo, M.; Sasamori, T.; Tokitoh, N.; Ogomi, Y.; Hayase, S.; Murata, Y. Reproducible Fabrication of Efficient Perovskite-Based Solar Cells: X-Ray Crystallographic Studies on the Formation of  $\text{CH}_3\text{NH}_3\text{PbI}_3$  Layers. *Chem. Lett.* **2014**, *43* (5), 711–713.
- (32) Guo, X.; McCleese, C.; Kolodziej, C.; Samia, A. C. S.; Zhao, Y.; Burda, C. Identification and Characterization of the Intermediate Phase in Hybrid Organic-Inorganic  $\text{MAPbI}_3$  Perovskite. *Dalton Trans.* **2016**, *45* (9), 3806–3813.
- (33) Ozaki, M.; Shimazaki, A.; Jung, M.; Nakaike, Y.; Maruyama, N.; Yakumar, S.; Rafieh, A. I.; Sasamori, T.; Tokitoh, N.; Ekanayake, P.; Murata, Y.; Murdey, R.; Wakamiya, A. A Purified, Solvent-Intercalated Precursor Complex for Wide-Process-Window Fabrication of Efficient Perovskite Solar Cells and Modules. *Angew. Chem., Int. Ed.* **2019**, *58* (28), 9389–9393.
- (34) Ozaki, M.; Nakaike, Y.; Shimazaki, A.; Jung, M.; Maruyama, N.; Yakumar, S.; Rafieh, A. I.; Ekanayake, P.; Saito, T.; Shimakawa, Y.; Sasamori, T.; Murata, Y.; Murdey, R.; Wakamiya, A. How to Make Dense and Flat Perovskite Layers for > 20% Efficient Solar Cells: Oriented, Crystalline Perovskite Intermediates and Their Thermal Conversion. *Bull. Chem. Soc. Jpn.* **2019**, *92* (12), 1972–1979.
- (35) Petrov, A. A.; Sokolova, I. P.; Belich, N. A.; Peters, G. S.; Dorovatovskii, P. V.; Zubavichus, Y. V.; Khrustalev, V. N.; Petrov, A. V.; Grätzel, M.; Goodilin, E. A.; Tarasov, A. B. Crystal Structure of DMF-Intermediate Phases Uncovers the Link between  $\text{CH}_3\text{NH}_3\text{PbI}_3$  Morphology and Precursor Stoichiometry. *J. Phys. Chem. C* **2017**, *121* (38), 20739–20743.
- (36) Guo, Y.; Shoyama, K.; Sato, W.; Matsuo, Y.; Inoue, K.; Harano, K.; Liu, C.; Tanaka, H.; Nakamura, E. Chemical Pathways Connecting Lead (II) Iodide and Perovskite via Polymeric Plumbate (II) Fiber. *J. Am. Chem. Soc.* **2015**, *137* (50), 15907–15914.
- (37) Stone, K. H.; Gold-Parker, A.; Pool, V. L.; Unger, E. L.; Bowring, A. R.; McGehee, M. D.; Toney, M. F.; Tassone, C. J. Transformation from Crystalline Precursor to Perovskite in  $\text{PbCl}_2$ -Derived  $\text{MAPbI}_3$ . *Nat. Commun.* **2018**, *9*, 3458.
- (38) Lee, B.; Hwang, T.; Lee, S.; Shin, B.; Park, B. Microstructural Evolution of Hybrid Perovskites Promoted by Chlorine and Its Impact on the Performance of Solar Cell. *Sci. Rep.* **2019**, *9*, 4803.

(39) Pham, N. D.; Tiong, V. T.; Chen, P.; Wang, L.; Wilson, G. J.; Bell, J.; Wang, H. Enhanced Perovskite Electronic Properties via a Modified Lead (II) Chloride Lewis Acid-Base Adduct and Their Effect in High-Efficiency Perovskite Solar Cells. *J. Mater. Chem. A* **2017**, *5* (10), 5195–5203.

(40) Xiao, M.; Huang, F.; Huang, W.; Dkhissi, Y.; Zhu, Y.; Etheridge, J.; Gray-Weale, A.; Bach, U.; Cheng, Y.-B.; Spiccia, L. A Fast Deposition-Crystallization Procedure for Highly Efficient Lead Iodide Perovskite Thin-Film Solar Cells. *Angew. Chem.* **2014**, *126* (37), 10056–10061.

(41) March, A. Mathematische Theorie Der Regelung Nach Der Korngestah Bei Affiner Deformation. *Kristallogr. Cryst. Mater.* **1932**, *81* (1–6), 285–297.

(42) Dollase, W. A. Correction of Intensities of Preferred Orientation in Powder Diffractometry: Application of the March Model. *J. Appl. Crystallogr.* **1986**, *19*, 267–272.

(43) Dinnebier, R. E.; Leineweber, A.; Evans, J. S. O. *Rietveld Refinement: Practical Powder Diffraction Pattern Analysis Using TOPAS*; De Gruyter, 2018; pp 50–51.

(44) Zolotoyabko, E. Determination of the Degree of Preferred Orientation within the March-Dollase Approach. *J. Appl. Crystallogr.* **2009**, *42* (3), 513–518.

(45) Takahashi, S.; Uchida, S.; Chatterjee, A.; Segawa, H. The Effect of Chloride Atoms to Induce Organohalide Perovskite Intermediate Crystal Phase: A Simulation Rationale. *Appl. Phys. Express* **2022**, *15* (7), 075504.

(46) Stoumpos, C. C.; Malliakas, C. D.; Kanatzidis, M. G. Semiconducting Tin and Lead Iodide Perovskites with Organic Cations: Phase Transitions, High Mobilities, and near-Infrared Photoluminescent Properties. *Inorg. Chem.* **2013**, *52* (15), 9019–9038.

(47) Grovenor, C. R. M. M. Grain Boundaries in Semiconductors. *Journal of Physics C: Solid State Physics* **1985**, *18* (21), 4079–4119.

(48) DeQuilettes, D. W.; Vorpahl, S. M.; Stranks, S. D.; Nagaoka, H.; Eperon, G. E.; Ziffer, M. E.; Snaith, H. J.; Ginger, D. S. Impact of Microstructure on Local Carrier Lifetime in Perovskite Solar Cells. *Science* **2015**, *348* (6235), 683–686.

(49) Momma, K.; Izumi, F. VESTA 3 for Three-Dimensional Visualization of Crystal, Volumetric and Morphology Data. *J. Appl. Crystallogr.* **2011**, *44* (6), 1272–1276.